Enhanced volcanic activity and long-term warmth in the middle Eocene revealed by mercury and osmium isotopes from IODP Expedition 369 Site U1514

Dhongil Lim[1,2*], Zhaokai Xu[3,4], Jihun Kim[1,2], Wei Wang[5], Emma Ownsworth[6], David Selby[6], Runsheng Yin[7], Taesoo Chang[8]

[1]Korea Institute of Ocean Science & Technology, Busan 49111, Korea

[2]Major of Ocean Sciences, University of Science & Technology, Daejeon 34113, Korea

[3]Key Laboratory of Marine Geology and Environment, Institute of Oceanology, Chinese Academy of Sciences, Qingdao 266071, China

[4]Laboratory for Marine Geology, Laoshan Laboratory, Qingdao 266061, China.

[5]Shenzhen Branch of China National Offshore Oil Corporation, Shenzhen 518000, China

[6]Department of Earth Sciences, Durham University, Durham DH1 3LE, UK.

[7]State Key Laboratory of Ore Deposit Geochemistry, Institute of Geochemistry, Chinese Academy of Sciences, Guiyang 550081, China

[8]Department of Geology, Chonnam National University, Kwangju 61186, Republic of Korea

*Corresponding authors: oceanlim@kiost.ac.kr

Abstract

Rapid plate reorganization may have influenced global climate during the Eocene; however, its linkage remains poorly constrained, particularly during the middle Eocene. To elucidate this tectonic–climatic relationship, here, we conducted a comprehensive analysis based on high-resolution mercury (Hg) and osmium (Os) abundance and isotope data obtained from the complete Eocene sedimentary sequence of Site U1514, drilled in the Mentelle Basin off southwest Australia. The Hg signals in this sedimentary sequence, which are characterized by significantly high enrichment and insignificant mass-independent fractionation (Δ^{199}Hg) signal, confirm that the middle Eocene (~45–38 Ma) was a period of persistent, increased volcanism, accompanied by intense tectonic activity. In particular, a remarkable seafloor volcanic eruption persisted for approximately 1.5 million years (~42.0–40.5 Ma), immediately preceding the Middle Eocene Climate Optimum (MECO). Contemporaneously, the

trends toward a slightly more radiogenic seawater $^{187}Os/^{188}Os$ (Os_i) composition denote the prevalence of intensified continental weathering under a warm, humid climate during the middle Eocene, a phenomenon particularly evident during the MECO. Importantly, the Hg and Os records from Site U1514 reveal the occurrence of a multi-million-year warming reversal amid the long-term Eocene cooling trend, which likely contributed to significant CO_2 reduction during the late Eocene. These findings significantly enhance our understanding of Eocene climate dynamics, which are fundamentally linked to intensive tectonic-driven volcanic activity and associated continental chemical weathering.

Keywords: Middle Eocene warmth; Hg and Os isotopes; volcanism; continental weathering; Site U1514

1. Introduction

The Eocene was a globally significant period marked by extensive global plate reorganization (Müller et al., 2016), as well as an Earth's climate shift from a warmhouse phase to a coolhouse phase (Zachos et al., 2001). In the southern high latitudes, the early and middle Eocene was marked by the extremely rapid separation of Australia from Antarctica through ridge extension and rifting on the Kerguelen Plateau and Broken Ridge (Royer and Sandwell, 1989; Veevers, 2000; Borissova et al., 2010). This plate tectonic activity would have led to massive ridge/arc volcanism and prolonged CO_2 outgassing (Jones and Fitzgerald, 1984; Rea et al., 1990 and references therein), which potentially triggered global warming and associated perturbations in the land–ocean system (Wang et al., 2022). However, most middle Eocene studies have concentrated primarily on specific warming periods, such as the Middle Eocene Climate Optimum (MECO) (e.g., Bohaty and Zachos, 2003; Westerhold et al., 2018; van der Ploeg et al., 2018; Henehan et al., 2020; van der Boon et al., 2021), leaving gaps in our understanding of the volcanic response to active tectonic movements during the middle Eocene and its environmental and climatic impacts. In addition, the mechanisms driving the MECO warming,

particularly the sudden rise in atmospheric CO_2, are debated (Bohaty and Zachos, 2003; van der Ploeg et al., 2018; Henehan et al., 2020).

A recent study proposed that the secular Cenozoic cooling trend in the southern mid-latitudes was interrupted by a multi-million-year warmth, likely induced by large-scale volcanic eruptions triggered by tectonic movements during the middle Eocene (Wang et al., 2022). The absence of apparent cooling through the middle to late Eocene in subequatorial regions (Evans et al., 2018) also raises the possibility of the global-scale middle Eocene warmth. The association of this long-term warmth with intensified continental weathering may provide clues regarding the causal mechanism of the drastic decline in atmospheric CO_2 across the late Eocene and the Eocene/Oligocene transition (EOT) (DeConto and Pollard, 2003; Inglis et al., 2015). However, conclusive evidence for long-term middle Eocene warmth in the form of sedimentary records linking active tectonic movements, volcanism, and chemical weathering remains elusive. Therefore, it is necessary to re-examine the long-term Eocene cooling trend that began at the Early Eocene Climatic Optimum (EECO).

Mercury (Hg) and osmium (Os) isotopes in sedimentary records are ideal indices of volcanic eruption and continental weathering intensity, respectively (e.g., Peucker-Ehrenbrink and Ravizza, 2000; Lu et al., 2017; Grasby et al., 2019). There is a growing agreement that Hg enrichment or anomalies in sedimentary successions are potential signatures of large volcanic eruptions (Grasby et al., 2016, 2019 and references therein), providing new insights into the relationship between volcanic activity and climate change (Sial et al., 2020 and references therein). Hg isotopes (e.g., Δ^{199}Hg), which are unlikely to be altered by post-depositional processes, have also been adopted as indicators of the volcanogenic origin of Hg enrichment (Blum et al., 2014; Grasby et al., 2019; Sial et al., 2020). The ^{187}Os/^{188}Os isotope ratio of seawater reflects the mass balance between two Os sources: unradiogenic Os (~0.12) from volcanic/hydrothermal inputs and radiogenic Os (~1.4) from weathered continental crusts (Peucker-Ehrenbrink and Ravizza, 2000). Thus, records of age-corrected

seawater Os isotope composition have been utilized as an effective tool to identify the effects of continental weathering feedback (Ravizza et al., 2001; Cohen et al., 2004; Dickson et al., 2015). Nevertheless, the availability of combined Hg and Os isotope data covering the entire Eocene, which could provide a broader understanding of the dramatic Eocene climate changes, is limited. In this study, we reconstructed high-resolution Hg and Os abundance and isotope records from the Eocene sedimentary sequence of Site U1514, drilled in the Mentelle Basin off southwestern Australia during International Ocean Discovery Program (IODP) Expedition 369 (Fig. 1), to define the long-term middle Eocene warmth and gain insights into the relationships among tectonics, volcanism, and continental weathering during the middle Eocene.

2. Samples and methods

During IODP Expedition 369, a continuous sedimentary sequence of Eocene was recovered at Site U1514 (paleolatitude ~60~50°S, Fig. 1a) in the Mentelle Basin off southwest Australia (Fig. 1b). The studied Eocene sedimentary interval at the site spans ~165 m (70–235 m core composite depth below sea floor, CCSF) of sediment and is dominated by light greenish gray clayey nannofossil ooze, sponge spicule-rich clay, nannofossil-rich clay, and clayey nannofossil chalk (Fig. 2). In this study, a total of 89 sediment samples from Site U1514 sequence, corresponding to Eocene-aged sediments of ~34–50 Ma, were analyzed for total organic carbon (TOC), total sulfur (TS), total inorganic carbon (TIC), and elemental abundances (i.e., Al, Fe, Mn, Mo, U, Hg, and Os), as well as Hg and Os isotopic compositions.

2.1. Total contents of inorganic carbon, organic carbon, sulfur, and other elements

The total carbon (TC) and total sulfur (TS) contents were measured using an elemental analyzer (FLASH 2000; Thermo Fisher Scientific, USA) and the total inorganic carbon (TIC) content was measured using a CO_2 coulometer (CM5014; UIC, Joliet, IL, USA). The total organic carbon (TOC)

content was calculated as the difference between the TC and TIC contents. For these components, relative deviations between measured and certified values of standard reference materials (L-cysteine for TC, BBOT for TS, and pure calcium carbonate for TIC), as well as their analytical reproducibility, were less than 5%, indicating satisfactory recoveries. For the concentrations of elements (Al, Fe, Mn, Mo, and U) for bulk sediments, each powdered sediment sample was fused with lithium metaborate ($LiBO_2$) flux and the molten beads were then poured into a volume of dilute nitric acid and stirred until dissolved. The resultant solutions were then analyzed using a combination of a Thermo ICAP 6500 radial inductively coupled plasma optical emission spectroscopy (ICP-OES) and Thermo Elemental X Series II ICP mass spectrometry (ICP-MS). Calibration for both instruments was achieved via matrix matched calibration standards produced from combinations of ICP-grade single element standards. Standard reference material (SBC-1), was analyzed together with a batch of sediment samples and the relative deviations between measured and certified values were less than 5–10 %.

2.2. Mercury concentration and a three-step sequential extraction

The mercury (Hg) concentrations of the sediment samples were determined using a mercury analyzer with thermal decomposition, amalgamation atomic absorption spectroscopy module (Hydra-C, a detection limit of 0.005 ng Hg; Teledyne Leeman Labs, Hudson, NH, USA) based on the US EPA method 7473. The analysis error, determined by repeated measurements of a standard reference material (MESS-3) together with a batch of sediment samples, was less than 3%, indicating satisfactory data acquisition. Hg enrichment factors (EF_{Hg}) were calculated as:

$$EF_{Hg} = (Hg/TOC)_{sample}/(Hg/TOC)_{bg}$$

where $(Hg/TOC)_{sample}$ and $(Hg/TOC)_{bg}$ represent the normalized Hg concentration of an individual sample and a reference background (bg) interval (i.e., early and late Eocene sediments for Site

U1514). The median Hg/TOC ratio was assigned as its reference background value; note that the median was used in preference to the mean owing to the sensitivity of the latter parameter to outlier values.

To better understand factors controlling of THg concentrations, a three-step sequential extraction scheme based on the procedures of Burt et al. (2003) was used to divide the carbonate- and Fe-Mn hydroxide-bound fraction (Fe-Mn hydroxide-bound Hg), organic matter- and sulfide-bound fraction (organic/sulfide-bound Hg), and residual faction (final residue-Hg). More detailed description for the sequential extraction was addressed in Kim et al. (2022).

2.3. Hg isotopes

All analytical procedures and measurements for Hg isotopes were performed at the isotope laboratory of Institute of Geochemistry, Chinese Academy of Sciences, Guiyang, China. A more detailed description for the analytical procedure can be found in Yin et al. (2016). In brief, the samples were prepared for Hg isotope analysis using a double-stage tube furnace coupled with 40% anti aqua regia (HNO_3/HCl = 2/1, v/v) trapping solutions. The solutions were diluted to 0.5 ng/mL with an acid concentration of 10–20% prior to Hg isotope analysis using a Neptune Plus multi-collector ICP-MS.

Mass dependent fractionation (MDF) of Hg isotopic results are expressed as delta (δ) values in units of per mille (‰) variation relative to the bracketed NIST SRM 3133 Hg standard, as follows:

$$\delta^{202}\mathrm{Hg} = [(^{202}\mathrm{Hg}/^{198}\mathrm{Hg})_{\mathrm{sample}}/(^{202}\mathrm{Hg}/^{198}\mathrm{Hg})_{\mathrm{standard}} - 1] \times 1000$$

Hg-isotopic values that did not follow the theoretical MDF were considered to exhibit isotopic anomalies caused by mass independent fractionation (MIF) (Bergquist and Blum, 2007). MIF values were calculated for ^{199}Hg and ex-pressed as per mille deviations from the predicted values based on the MDF law:

$$\Delta^{199}Hg \approx \delta^{199}Hg - \delta^{202}Hg \times 0.252$$

The analytical uncertainties of Hg isotopic compositions were evaluated by repeated analysis of the isotopic compositions of NIST-3177 (n = 6) and GSS-4 (n = 6). The overall average and uncertainty of NIST-3177 (δ^{202}Hg: –0.55 ± 0.09‰; Δ^{199}Hg: −0.02 ± 0.05‰, 2SD), and GSS-4 (δ^{202}Hg: −1.70 ± 0.07‰; Δ^{199}Hg: –0.46 ± 0.02‰, 2SD) agree with previously published results (Yin et al., 2022; Chen et al., 2022).

2.4. Re-Os abundance and isotope analytical protocol

All rhenium (Re) and osmium (Os) isotope analyses were performed at the Durham Geochemistry Centre, Durham University (UK). A more detailed description of the analytical procedure can be found in van der Ploeg et al. (2018). In brief, powdered samples of approximately ~1 g were loaded into Carius tubes with a known amount of mixed ^{185}Re + ^{190}Os tracer solution (spike), and 8 mL of CrO_3–H_2SO_4 solution, sealed and then heated in an oven at 220 °C for 48 hrs. Osmium was isolated from the CrO_3–H_2SO_4 sample solution by using solvent extraction ($CHCl_3$), and then back extracted by hydrobromic acid (HBr), and then further purified through micro distillation. Rhenium was isolated from the Os extracted CrO_3–H_2SO_4 sample solution by solvent extraction using sodium hydroxide (NaOH) and acetone (C_3H_6O), and anion chromatography. Following purification, the Re and Os fractions were loaded onto Ni and Pt filaments, respectively, together with 0.5 µL $BaNO_3$ and BaOH activator solutions, respectively. Rhenium and Os isotope ratios were determined by negative thermal ionization mass spectrometry, using Faraday cups for Re and a Secondary Electron Multiplier for Os in peak-hopping mode on a ThermoScientific Triton mass spectrometer.

The $^{187}Os/^{188}Os_{initial}$ ratios (Os_i) were calculated by correcting for post-depositional ^{187}Re decay over time with the following equation:

$$^{187}Os/^{188}Os_{initial}\ (Os_i) = {}^{187}Os/^{188}Os_{measured} - {}^{187}Re/^{188}Os_{measured} \times (e^{\lambda t} - 1)$$

where λ is the ^{187}Re decay constant ($1.666 \cdot 10^{-11}$ yr^{-1}) and *t* is ages of the studied samples for Site U1514. Procedural blanks were 9.6 ± 1.0 pg for Re and 0.04 ± 0.05 pg for Os, with a $^{187}Os/^{188}Os$ ratio of 0.20 ± 0.05 (1SD; n = 4). The $^{187}Re/^{188}Os$ and $^{187}Os/^{188}Os$ uncertainties (2SE) include full propagation of uncertainties in weighing, mass spectrometer measurements, spike calibrations, blank corrections, and reproducibility of standards. Analytical precision for the lab was monitored through repeated analysis of 50 pg DROsS and 125 pg ReSTD solution standards, which yield a running average of 0.1608 ± 0.0006 (1SD; n = 916) for $^{187}Os/^{188}Os$ and 0.5986 ± 0.0015 (1SD; n = 784) for $^{185}Re/^{187}Re$.

3. Results

The chronostratigraphic framework of the studied interval at IODP 369 Site U1514 was constrained by linear interpolation between age points obtained from shipboard biostratigraphy and magnetostratigraphy studies (Fig. 2). More information about age-depth model for Site U1514 section is given in Wang et al. (2022). Linear sedimentation rates were much higher (1.20–1.85 cm/kyr) during the middle Eocene (~45–38 Ma) than during the early and late Eocene (0.40–0.90 cm/kyr). All analytical results of this study are summarized in Supplementary Tables S1–S4. The TOC and TS contents were less than ~0.30% and ~0.11%, respectively, with limited variation. The Al, Fe, Mn, Mo, and U concentration ranges were 10.0–52.7 mg/g, 7.2–34.6 mg/g, 140–1403 μg/g, 0.09–1.54 μg/g, and 0.18–1.45 μg/g, respectively. No distinct variation in Al, Fe, Mn, Mo, and U concentrations was observed across the studied interval (Supplementary Table S2). Total Hg concentrations in the Eocene sediments of Site U1514 ranged from ~1 to 246 ng/g, with a significant increase during the middle Eocene, featuring peaks exceeding 100 ng/g (Fig. 3a). Similar temporal trends were observed in Al-, TIC-, TOC-, and TS-normalized Hg concentrations (Fig. 3b, c).

Sequential extraction data showed that sedimentary Hg was present primarily in organic matter fraction (range: 46–89% of the total concentration, average: 64 ± 11%), followed by the Fe-Mn hydroxide-bound (range: 6–39%, average: 22 ± 9%) and residual fractions (range: 4–23%, average: 14 ± 6%) (Supplementary Fig. S1).

Hg mass-dependent fractionation (δ^{202}Hg) values from Site U1514 sediments ranged from −1.74 to +0.86 ‰, with the majority falling between −1.15 and −0.11‰ (Supplementary Table S3). In general, Hg undergoes a series of complex physical, chemical, and biological transformations in the environment, potentially leading to ambiguous interpretations (Blum et al., 2014). Therefore, we did not interpret δ^{202}Hg record and instead focused on Hg mass-independent fractionation (Δ^{199}Hg) signals, providing clearer insights into the sources of Hg due to their conservation through post-depositional processes. The Δ^{199}Hg values from Site U1514 sediments ranged from +0.04 to +0.25‰ (Fig. 3d), indicating variation several times greater than the analytical uncertainty (2SD = 0.05). With the exception of samples from specific periods with high Hg concentration peaks, exceeding ~100 ng/g, during the middle Eocene, Δ^{199}Hg values exhibited limited variability, typically ranging between +0.15 and +0.23‰, suggesting a relatively constant background level (+0.18 ± 0.05‰) across the studied sedimentary section. However, the middle Eocene strata exhibited abrupt and significant drops towards near-zero Δ^{199}Hg values, particularly in samples associated with high Hg concentration peaks (Fig. 3d).

Rhenium (Re) and Os abundance and isotopic composition varied considerably in the studied samples. The Re and total Os, and ^{192}Os (the "common" Os component) concentration ranges were 0.03–1.28 ng/g, 22.61–167.77 pg/g, and 8.89–65.77 pg/g, respectively (Supplementary Table S4), with a significant increase occurring during the middle Eocene (Fig. 3e). The ^{187}Re/^{188}Os and ^{187}Os/^{188}Os ratios varied from 2.07 to 76.95 and 0.47 to 0.59, respectively (Supplementary Table S4). Initial seawater ^{187}Os/^{188}Os (Os_i) values calculated using the assigned ages of each sample ranged

from 0.47 to 0.57, featuring a significant shift toward more radiogenic composition between ~43 and 38 Ma, with maximum values at ~40.5–40 Ma (Fig. 3f). The early and late Eocene samples exhibited relatively less radiogenic characteristics, with Os_i values of 0.47–0.50; however, these values increased in the middle Eocene samples, ranging from 0.53 to 0.57. Although the magnitude of the positive Os_i shift at Site U1514 is small (~0.05), it exceeds the maximum analytical uncertainty (2SE = 0.005) by a factor of ~10. The Os_i values from Site U1514 were only moderately radiogenic, but significantly lower than those of present-day seawater (i.e., ~1.04–1.07, Peucker-Ehrenbrink and Ravizza, 2000). The Os_i record from Site U1514 is in good agreement with data from CD29-2 (Klemm et al., 2005), Pacific manganese crust (Burton, 2006), as well as ODP Site 865, in terms of values and broad temporal trends (Fig. 3f, Supplementary Fig. S2, see Fig. 1a for sample locations).

4. Discussion

4.1. Enhanced middle Eocene volcanism

Large volcanic eruptions in geological history have often led to anomalously high Hg enrichment or spikes in stratigraphic records, providing insights into their timing, duration, and intensity (e.g., Sial et al., 2016; Percival et al., 2018; Grasby et al., 2019; Shen et al., 2019, 2023). Accurate estimation of background Hg levels is a prerequisite for deepening our understanding of the distinctive features and nuanced variations in Hg records from the geological past, particularly because Hg anomalies may not always provide definitive signatures of enhanced volcanic emissions (Grasby et al., 2019 and references therein). The middle Eocene interval (~45–38 Ma) in Site U1514 geological record exhibits significantly elevated Hg concentrations, reaching ~250 ng/g with peaks exceeding 100 ng/g around 42–40.5 Ma (Fig. 3a). These concentrations markedly exceed the background level of 11 ng/g (i.e., the average for early and late Eocene intervals) in the Site U1514 section (Fig. 3a), the average value of 50 ng/g for the upper continental crust (Rudnick and Gao,

2014), and the mean Hg value in sediments from several extinction and oceanic anoxic event zones (62.4 ng/g, Grasby et al., 2019), suggesting substantial Hg inputs during the middle Eocene. Furthermore, Hg concentrations during the middle Eocene, particularly in the period of 42–40.5 Ma, greatly surpass the organic-matter drawdown capacity limit (e.g., Hg = $48.5TOC^{0.89}$ or $150TOC^{0.89}$, Grasby et al. 2019), potentially supporting increased Hg loading during this period.

To further clarify the cause of elevated Hg concentrations observed in Site U1514 sedimentary records, it is necessary to normalize the data to the dominant Hg sequestration factor (Shen et al., 2020). Hg concentrations for Site U1514 sediments are primarily controlled by organic matter, as shown by the strong positive correlation between Hg and TOC (r^2 = ~0.5), but weak or no correlation (r^2 < 0.2) with TIC, TS, and Al concentrations, and Fe/Al and Mn/Al ratios (Supplementary Fig. S3). This finding was further supported by the predominance of organic/sulfide-bound Hg (64 ± 11% of the total concentration), which was significantly correlated with TOC (r^2 = ~0.5), but not with TS (Supplementary Fig. S1), indicating that organic matter played an essential role in the Hg depositional pathway at Site U1514. Redox conditions played a limited role in Hg enrichment in the Site U1514 sedimentary sequence, as indicated by low sulfur content (< 0.1%) and non-significant correlations with redox elemental proxies (TS, Mo/Al, and U/Al) (Supplementary Fig. S3). Similar temporal trends were observed in Al-, TIC-, TOC-, and TS-normalized Hg concentrations (Fig. 3b, c), suggesting that local depositional environments (e.g., grain size and sedimentation rate) are unlikely to be the primary factors controlling variation in Hg deposition at Site U1514. As such, the increased environmental Hg loading at Site U1514 can be estimated by values normalized to organic matter content (i.e., Hg/TOC). Site U1514 exhibited significantly elevated values of Hg/TOC (~200–760 ng/g/wt%), Hg enrichment factor (EF_{Hg}, ~4–16), and Hg flux (5–25 × 10^2 μg/m^2/kyr) throughout the middle Eocene (Fig. 4a–c). The Hg/TOC values greatly exceeded the background level of 96 ng/g/wt% (i.e., the average of samples with TOC > 0.2% for early and late Eocene intervals) in Site

U1514 record and the anomalous enrichment threshold (72 ng/g/wt%) derived from sedimentary records of major extinction and oceanic anoxic events (Grasby et al., 2019). This Hg increase during the middle Eocene was further supported by elevated EF_{Hg} values (Fig. 4b), where $EF_{Hg} > 2$ indicates significant Hg enrichment, implying a volcanic source of Hg in geologic successions (e.g., Shen et al., 2019). These results indicate that excess Hg inputs during the middle Eocene were likely driven by volcanism rather than increased organic matter flux (i.e., organic-matter Hg drawdown) and/or increased runoff. Notably, we identified an intense volcanic episode lasting for 1.5 Myr (42.0–40.5 Ma) and three shorter periods of volcanic activity at ~45.5, ~44, and ~39 Ma (Fig. 4a–c).

Conclusive evidence for such a volcanic Hg source was provided by paired Hg enrichment and isotope measurement (Fig. 5). Site U1514 sediments yielded Δ^{199}Hg values ranging from +0.04 to +0.25‰ (0.16 ± 0.06‰), with several peaks showing low values of up to +0.04‰ in the middle Eocene (Fig. 4d), comparable to that (−0.30 to +0.27‰) derived from extinction event records (Grasby et al., 2019). Generally, geogenic Hg sources exhibit negligible Hg mass-independent fractionation signatures (Δ^{199}Hg ~0‰) (Sherman et al., 2009). However, recent studies proposed that small, positive Δ^{199}Hg values in deep water environments may result from the deposition of Hg^{2+} absorbed from the atmosphere by volcanic plume particles rather than direct atmospheric deposition (Gong et al., 2017; Grasby et al., 2017, 2019). Such deposition is also likely in the deep-water basin of Site U1514, which displayed limited Δ^{199}Hg variability, except for Hg isotope spikes, and an overall slightly positive background value (+0.18 ± 0.05‰). Similar Hg signatures for dominant volcanic Hg enrichments are reported for the latest Permian extinction and Ordovician–Silurian extinction successions (Gong et al., 2017; Grasby et al., 2017). Interestingly, Δ^{199}Hg values at Hg peaks (i.e., ~45.5, ~44, ~39, and ~42.0–40.5 Ma) of the middle Eocene showed a significant shift toward values close to zero (Figs. 4, 5), indicating elevated Hg loading, likely attributable to increased seafloor volcanic activity, such as ridge volcanism and/or hydrothermal activity, which

typically exhibit near-zero Δ^{199}Hg values (Zambardi et al., 2009; Kim et al., 2022). Although such shifts in Δ^{199}Hg can result from a mix of terrestrial (highly negative Δ^{199}Hg) and seawater-sourced Hg (positive Δ^{199}Hg) (Sial et al., 2020; Shen et al., 2022), these sources are unlikely to explain the identical trend between Δ^{199}Hg and Hg enrichments and their negative correlation in this study (Fig. 5). Hg concentrations also showed no significant relationship with terrestrial-indicative Al content (Supplementary Fig. S3). Therefore, the Hg isotopic signals at Site U1514 indicate a sustained increase in widespread subaerial volcanism during the middle Eocene, with notable periods (particularly 42.0–40.5 Ma) marked by intensive pulses of seafloor volcanic/hydrothermal eruptions. This conclusion is further supported by the higher deposition of volcanic materials in the Mentelle Basin during the middle Eocene (43–38 Ma) (Wang et al., 2022).

Although there are no candidates for a large igneous provenance event in the geological record coincident with the middle Eocene (Sluijs et al., 2013; Ernst et al., 2021), increased volcanism appears to be associated with active plate tectonic reorganization (e.g., the rifting of Australia from Antarctica, the resumption of Pacific subduction, and the closing of Neotethys), and large igneous activity in southeastern Australia as well (Fig. 4f). Significant increase in arc/mid-ocean ridge volcanism and hydrothermal activity during the middle Eocene (~35–45 Ma) have been also identified in the North Atlantic (Rea et al., 1990) and in various other regions (van der Ploeg et al., 2018). Both volcanism and hydrothermal activity would have been much more intense during continental rifting and plate boundary rearrangements of middle Eocene (Jones and Fitzgerald, 1984; Rea et al., 1990 and references therein).

4.2. Volcanic climaxes and short-lived warming events

The Eocene epoch was distinguished by extensive global plate reorganization, including the abruptly accelerated separation of Australia and Antarctica at ~45–43 Ma and rifting of the Kerguelen

Plateau and Broken Ridge caused by the onset of seafloor spreading at the Southeast Indian Ridge at ~43–40 Ma (Veevers, 2000; Li et al., 2003). This tectonic activity would have been accompanied by extensive seafloor volcanism/hydrothermal activity in the Mentelle Basin and on the Naturaliste Plateau (Jones and Fitzgerald, 1984; Rea et al., 1990 and references therein; Borissova et al., 2010), as well as at the Ninety East Ridge (Fleet and McKelvey, 1978). Igneous activity in southeastern Australia peaked between 45 and 37 Ma (Fig. 4f) and around Antarctica at ~45 Ma (Wang et al., 2009). Major volcanic climax records (i.e., 45.5, 44, and 42.0–40.5 Ma) interpreted from Site U1514 should accurately depict such a tectonic history in the Southern Ocean. Notably, the series of intense volcanic eruptions that persisted for ~1.5 Myr (42.0–40.5 Ma) coincided with the period of greatest separation between Australia and Antarctica. Additionally, these eruptions correspond to the warming event known as the Late Lutetian Thermal Maximum (LLTM, ~41.5 Ma), which is mainly documented in high-latitude Atlantic sites (Westerhold et al., 2018; Rivero-Cuesta et al., 2020). High insolation forcing has been thought to underlie the LLTM (Westerhold et al., 2018 and reference therein); however, our findings suggest that the greatly increased volcanic eruptions in the Southern Ocean during this period are a plausible alternative mechanism for this transient warming.

The MECO, a transient global warming event that occurred at ~40.5–40 Ma in association with an abrupt rise in atmospheric CO_2 (Sluijs et al., 2013), was first recognized through a ~1‰ negative oxygen isotope excursion in bulk carbonate and benthic foraminiferal tests in Southern Ocean cores (Bohaty and Zachos, 2003), and subsequently identified in the Atlantic Ocean and the central western Tethys Ocean (Boscolo Galazzo et al., 2014 and references therein). Although a causal relationship between volcanism and MECO warming has been suggested for some areas (e.g., van der Ploeg et al., 2018; van der Boon et al., 2021 and references therein), a plausible source of excess volcanic CO_2 remains to be identified, particularly in the high southern latitudes. In the Site U1514 record, the potential MECO period was identified by pronounced negative excursions in the $\delta^{13}C$ value (Wang et

al., 2022) (Fig. 4e). Hg enrichment remained high throughout the MECO period; however, there were no notable Hg peaks or isotope spikes corresponding to the period of negative carbon excursions, implying the absence of catastrophic explosive volcanic eruptions (Fig. 4). Another likely explanation for the absence of MECO Hg spikes in this area is dilution by the highest influx of terrigenous materials during this period, revealed by Os_i isotope signals with an abrupt increase during the MECO at Site U1514 (discussed below). The intensified continental weathering suggests significant rise in temperature and atmospheric CO_2 concentrations during this interval (Wang et al., 2022). Nevertheless, the MECO was likely triggered by an abrupt, massive volcanic climax that persisted for ~1.5 Myr (42.0 and 40.5 Ma) prior to its onset. These data support previous hypotheses (e.g., Bohaty and Zachos, 2003) that enhanced volcanic activity associated with plate tectonics in the Southern Ocean could explain contradictory global warming events (e.g., short-lived pulses of CO_2) during the middle Eocene (i.e., LLTM and MECO).

4.3. Increased continental weathering and long-term middle Eocene warmth

The overall enhanced long-term volcanic activity during the middle Eocene, observed from Hg proxy records from Site U1514 (Fig. 4), should have resulted in massive pCO_2 emissions, with subsequent warming and environmental perturbations (e.g., Percival et al., 2016). This volcanism–climate warming feedback can be explained by the facilitation of continental chemical weathering by elevated CO_2 levels and a warm and humid climate, i.e., the silicate weathering thermostat hypothesis (Cohen et al., 2004; Dickson et al., 2015; Penman et al., 2020). Initial seawater $^{187}Os/^{188}Os$ ratio (Os_i) has been used as a powerful tool for reconstructing continental weathering changes in geological successions involving hyperthermal climate events (e.g., ocean anoxic events, Paleocene–Eocene Thermal Maximum, and Triassic–Jurassic transition) (Peucker-Ehrenbrink and Ravizza, 2000; Du Vivier et al., 2014; Dickson et al., 2015 and references therein; Percival et al., 2016; Shen et al.,

2023). These studies are ultimately based on the proportional mixing of fluxes of two end-member Os isotope components: terrestrial ($^{187}Os/^{188}Os$ of ~1.4) and volcanic–hydrothermal inputs ($^{187}Os/^{188}Os$ of ~0.13). The Os_i record from Site U1514 exhibited a significant positive shift toward more radiogenic values during the middle Eocene (~43.5–38 Ma), with enhanced volcanism (Figs. 3f, 6a). This overall Os_i increase during the middle Eocene was also observed in sediment and manganese crust records from other sites, indicating that it is a global phenomenon (Supplementary Fig. S2).

Considering the relative invariability of both the Os_i record and ^{192}Os abundance data (Fig. 3), the balance of Os fluxes to the oceans and its uptake in organic matter did not change appreciably over time. Thus, the Os_i increase over the middle Eocene indicated in Site U1514 record may have been caused by decreased volcanic/hydrothermal activity and/or increased weathering of felsic radiogenic continental rocks. Given that Hg proxy signals at Site U1514 provide compelling evidence of a significant increase in volcanism during the middle Eocene, the increase in Os_i is more easily reconciled with a notable increase in continental silicate weathering. This suggestion is corroborated by a notable increase in terrigenous inputs from the Australian continent during the middle Eocene, indicated by a higher mass accumulation rate of siliciclastic fractions (Fig. 6b). Therefore, this definite Os_i shift during the middle Eocene reflects the sequestration of hydrogenous Os derived from the continent as a result of high weathering rates (Peucker-Ehrenbrink and Ravizza, 2000; Cohen, 2004; Percival et al., 2016). An analogous increase in radiogenic Os was also apparent in another geological period (Oceanic Anoxic Event 1a) around the study area (ODP Site 763), which has been interpreted as a sign of enhanced continental weathering triggered by global warming resulting from outgassing during volcanic episodes at the Kerguelen Plateau (Matsumoto et al., 2022).

Based on a simple mixing model calculation (Dickson et al., 2015), radiogenic Os fluxes increased by ~10–30% during the middle Eocene, indicating a coeval increase in the supply of

terrigenous materials into the study area. The large increase in the mass accumulation rate of the siliciclastic fraction during this period from ~0.4 to 1.2 g/cm^2/kyr supports our conclusion (Fig. 6b). At Site U1514, strengthened chemical weathering and leaching of source rocks were also corroborated by changes in indicators of the relative intensity of chemical weathering, i.e., an abrupt increase in the kaolinite/smectite ratio and a decrease in the Mg/Al ratio between 43 and 38 Ma (Fig. 6c). The presence of subtropical to tropical rainforests in southwestern Australia during the middle Eocene implies that there was considerable continental precipitation and runoff (Martin, 2006), which likely facilitated sufficient hydrolysis for chemical weathering. Accordingly, the compelling evidence in records of Os_i, elemental indices, terrigenous input fluxes, and climate conditions indicates the intensification of continental weathering during the middle Eocene on the Australian continent, possibly driven by a warm, wet climate (Wang et al., 2022). Notably, the overall increase in Os_i values during the middle Eocene at other sites (Supplementary Fig. S2) indicates a global enhancement in continental weathering during this period, despite slight differences in absolute Os_i values between sites, possibly due to differences in coastal proximity and oceanographic setting (Paquay and Ravizza, 2012; Du Vivier et al., 2014). Globally enhanced chemical weathering during the middle Eocene has also been inferred from lead ($^{206}Pb/^{207}Pb$) and neodymium (εNd) isotope records (Burton, 2006).

Our analysis of Hg and Os isotope records, along with previously reported elemental and Sr isotope data (Wang et al., 2022), verify a distinct, prolonged middle Eocene warmth that persisted for ~5 Myr (~43–38 Ma, Fig. 6) in the southern mid-high latitudes. This long-term warmth period, possibly triggered by plate tectonics–volcanism–rising CO_2 feedback, challenges the prevailing notion of a continuous Eocene cooling phase following the early Eocene. Nevertheless, this middle Eocene warming reversal is reconciled with overall increasing trends in global deep-sea water and Austral high latitude surface water temperatures (Fig. 6d), as well as the absence of cooling

throughout the Eocene in tropical regions (Evans et al., 2018). This finding implies that long-term Eocene cooling occurred at higher latitudes than previously thought, such as pole regions. The overall intensified continental weathering during this global warming period may have contributed to the prolonged reduction of atmospheric CO_2, in turn potentially leading to late Eocene cooling and/or EOT glaciation (DeConto and Pollard, 2003; Anagnostou et al., 2016; Cramwinckel et al., 2018). Thus, our findings support tectonic-induced CO_2 forcing, rather than changes in ocean circulation through ocean gateway reorganization or paleogeographic change, as the main driver of Eocene climate (Inglis et al., 2015; Cramwinckel et al., 2018).

4.4. The MECO pulse in continental weathering

Close links among volcanism, continental chemical weathering, and climate warming were also evident in the MECO interval from Site U1514, with the greatest shift toward more radiogenic Os_i compositions (Fig. 6a). The highest radiogenic Os signal during this interval signifies that the influx of weathered terrestrial material in response to the inferred CO_2 rise and warming was most prominent during the MECO period, which is in good agreement with predictions based on the silicate weathering thermostat hypothesis. In particular, a coeval warming phase with increased sea surface temperatures (~28°C during the peak of the MECO event) was identified on the Tasman Plateau in eastern Australia (Bijl et al., 2013). This result supports the MECO as a period of hydrological cycle intensification and more extensive flooding on the western Australian continent (Wang et al., 2022). Furthermore, the rapid (10s of kyr) temperature drop after the MECO warming peak can be explained by greatly strengthened silicate weathering during this warming period, supporting the reactivation of the silicate weathering feedback after the hypothesized gradual decline during the Eocene (Henehan et al., 2020). Interestingly, the MECO record of Os_i at Site U1514 is in conflict with the results from other MECO sedimentary successions (i.e., Site U1333, Site 959, and

Site 1263), exhibiting a slight Os_i decrease (van der Ploeg et al., 2018) (Fig. 6a, Supplementary Fig. S2). A relative increase in volcanic–hydrothermal input is required to explain this abrupt shift to unradiogenic Os_i value, (Peucker-Ehrenbrink and Ravizza, 2000; Du Vivier et al., 2014). However, van der Ploeg et al. (2018) considered this decrease in Os_i across the MECO to be caused by relatively weakened silicate weathering, which resulted in prolonged accumulation of volcanic CO_2 in the oceans and atmosphere during this period. This scenario fails to account for a rapid drop in temperatures following the peak of the MECO warming trend, potentially triggered by the reactivation of silicate weathering feedback after million years of hypothesized gradual decline. Although the regional disparity (i.e., heterogeneous seawater Os isotope composition) in Os_i values likely arises from differing environmental settings, including a restricted basin, and/or a more proximal depositional setting at the time of deposition (Du Vivier et al., 2014), this spatial heterogeneity (i.e., contrasting pattern) of Os isotope signals in MECO sedimentary successions requires further investigation with additional data from other locations. Nonetheless, the abrupt increase to more radiogenic Os_i at Site U1514 is difficult to explain without invoking enhanced continental weathering rates (Peucker-Ehrenbrink and Ravizza, 2000; Percival et al., 2016). Although the possibility of unradiogenic Os input from enhanced volcanism during the middle Eocene cannot be excluded, a substantial amount of terrigenous detritus from the Australian continent may have overwhelmed the seawater Os isotope composition, thereby masking volcanic-induced isotope signals, and by inference of the Os_i of the deposited sediments. This hypothesis may explain why the MECO thermal maximum interval at Site U1514 was characterized by the largest increase in Os_i values. Thus, in some cases, silicate weathering feedback may obscure volcanic isotope signals, limiting our understanding of the geographic distribution and global correlation of volcanic events.

5. Conclusions

We have documented the complete Eocene variations of Hg and Os concentrations and their isotope signals from Site U1514, which provide compelling evidence of the operation of feedback between plate tectonics, volcanism, continental chemical weathering, and climate change during the middle Eocene. A comprehensive analysis of Hg and Os isotopes demonstrated that the middle Eocene (~45–38 Ma) experienced extensive volcanic activity, evident from notably elevated Hg enrichments and near-zero Δ^{199}Hg values. This prolonged and enhanced volcanic activity was intricately linked to widespread plate tectonic activity in the Southern Ocean, and likely played a crucial role in triggering global warming incidents, including the LLTM and MECO. An analysis of seawater ^{187}Os/^{188}Os (Os$_i$) in conjunction with supporting data, such as influxes in terrigenous materials and elemental indices, underscores that the middle Eocene was a critical period in the intensification of the continental weathering response to CO_2 rise and warming. This intensified continental weathering was most prominent during the MECO warming, further supporting the prevalence of warmer, more humid climate conditions. Notably, our findings suggest a long-term (~ 5 Myr) middle Eocene warming, instigated by a feedback loop involving plate tectonics and volcanic activity in the southern high latitudes. This finding challenges the prevailing notion of a continuous global cooling trend throughout the Eocene; however, the prolonged continental weathering during this long-term warmth is reconcilable with the reduced atmospheric CO_2 levels that contributed to late Eocene cooling and/or EOT glaciation.

CRediT authorship contribution statement

All authors have contributed to this work. **D. Lim:** Conceptualization, Methodology, Funding acquisition, Investigation, Writing – original draft, Writing – review & editing; **Z. Xu:** Conceptualization, Funding acquisition, Writing – review & editing; **J. Kim:** Investigation, Methodology; Formal analysis; **D. Selby, E. Ownsworth, and W. Wang:** Investigation, Methodology,

Writing – review & editing; **R. Yin:** Methodology, Writing – review & editing; **T. Chang:** Writing – review & editing. All authors have seen and approved manuscript.

Declaration of competing interest

The authors declare that they have no known competing financial interests or personal relationships that could have appeared to influence the work reported in this paper.

Data availability

The original contributions presented in the study are given in the article/Supplementary Material.

Acknowledgements

This study was supported by the National Research Foundation of Korea (2021R1A2C1014443 and 2021R1I1A2059972), the National Key Research and Development Program of China (2022YFF0800503), and the Strategic Priority Research Program (XDB42000000 and XDB40010100) of the Chinese Academy of Sciences. Chris Ottley and Geoff Nowell are acknowledged for laboratory support. Finally, we thank Dr. Peucker-Ehrenbrink and an anonymous reviewer for helpful input on the manuscript.

Appendix A. Supplementary material

Supplementary material related to this article can be found on-line at https://doi.org/xxxxxxxxxxxxx.

References

Anagnostou, E., John, E.H., Edgar, K.M., Foster, G.L., Ridgwell, A., Inglis, G.N., Pancost, R.D., Lung, D.J., Pearson, P.N., 2016. Changing atmospheric CO_2 concentration was the primary

driver of early Cenozoic climate. Nature 533, 380 – 384. https://doi.org/10.1038/nature17423.

Bergquist, B.A., Blum, J.D., 2007. Mass-dependent and -independent fractionation of Hg isotopes by photoreduction in aquatic systems. Science 318, 417–420. https://doi.org/10.1126/science.1148050.

Bijl, P.K., Bendle, J.A.P., Bohaty, S.M., Pross, J., Schouten, S., Tauxe, L., Stickley, C.E., et al., 2013. Eocene cooling linked to early flow across the Tasmanian Gateway. Proc. Natl. Acad. Sci. U. S. A. 110, 9645–9650. https://doi.org/10.1073/pnas.1220872110.

Blum, J.D., Sherman, L.S., Johnson, M.W., 2014. Mercury isotopes in earth and environmental sciences. Annu. Rev. Earth Planet. Sci. 42, 249–269.

Bohaty, S.M., Zachos J., 2003. Significant Southern Ocean warming event in the late middle Eocene. Geology 31, 1017–1020. https://doi.org/10.1130/G19800.1.

Borissova, I., Bradshaw, B., Nicholson, C., Struckmeyer, H., Payne, D., 2010. New exploration opportunities on the southwest Australian margin–deep-water frontier Mentelle Basin. J. Aus. Pet. Prod. Explor. Assoc. 50, 47–60. https://doi.org/10.1071/AJ09004.

Boscolo Galazzo, F., Thomas, E., Pagani, M., Warren, C., Luciani, V., Giusberti, L., 2014. The middle Eocene climatic optimum (MECO): A multiproxy record of paleoceanographic changes in the southeast Atlantic (ODP Site 1263, Walvis Ridge). Paleoceanography 29, 1143–1161. https://doi:10.1002/2014PA002670.

Burton, K.W., 2006. Global weathering variations inferred from marine radiogenic isotope records. J. Geochem. Explor. 88, 262–265.

Burt, R., Wilson, M.A., Keck, T.J., Dougherty, B.D., Strom, D.E., Lindahl, J.A., 2003. Trace element speciation in selected smelter-contaminated soils in Anaconda and deer Lodge Valley, Montana, USA. Adv. in Environ. Res. 8, 51–67. https://doi.org/10.1016/S1093-0191(02)00140-5.

Chen, D. Ren, D., Deng, C., Tian, Z., Yin, R., 2022. Mercury loss and isotope fractionation during high-pressure and high-temperature processing of sediments: Implication for the behaviors of mercury during metamorphism. Geochim. Cosmochim. Acta 334, 231-240. https://doi.org/10.1016/j.gca.2022.08.010

Cohen, A.S., Coe, A.L., Harding, S.M., Schwark, L., 2004. Osmium isotope evidence for the regulation of atmospheric CO_2 by continental weathering. Geology 32, 157–160. https://doi.org/10.1130/G20158.1.

Cottin, J.-Y., MiChon, G., DelpeCh, G., 2011. The Kerguelen volcanic Plateau: the second largest oceanic Igneous Province (LIP) on earth and a witness of the Indian Ocean opening, in: The Kerguelen Plateau: Marine Ecosystems and Fisheries 2011, 35, pp. 29–42.

Cramwinckel, M.J., Huber, M., Kocken, I.J. et al., 2018. Synchronous tropical and polar temperature evolution in the Eocene. Nature 559, 382–386. https://doi.org/10.1038/s41586-018-0272-2.

DeConto, R. M., Pollard, D., 2003. Rapid Cenozoic glaciation of Antarctica induced by declining atmospheric CO_2. Nature 421, 245–249. https://doi.org/10.1038/nature01290.

Dickson, A.J., Cohen, A.S., Coe, A.L., Davies, M., Shcherbinina, E.A., Gavrilov, Y.O., 2015. Evidence for weathering and volcanism during the PETM from Arctic Ocean and Peri-Tethys osmium isotope records. Palaeogeog. Palaeoclimatol. Palaeoecol. 438, 300–307. http://dx.doi.org/10.1016/j.palaeo.2015.08.019.

Du Vivier, A.D.C., Selby D., Sageman, B.B., Jarvis, I., Gröcke, D.R., Voigt, S., 2014. Marine 187Os/188Os isotope stratigraphy reveals the interaction of volcanism and ocean circulation during Oceanic Anoxic Event 2. Earth Planet. Sci. Lett. 389, 23–33. http://dx.doi.org/10.1016/j.epsl.2013.12.024.

Ernst, E.R., Bond, D.P.G., Zhang, S.H., Buchan, K.L., Grasby, S.E., Youbi, N., Bilali, H.E., Bekker, A., Doucet, L.S., 2021. Large Igneous Province Record Through Time and Implications for Secular Environmental Changes and Geological Time-Scale Boundaries, in: Large Igneous Provinces: A Driver of Global Environmental and Biotic Changes, AGU Geophysical Monograph 255, pp. 1–26.

Edgar, K.M., MacLeod, K.G., Hasegawa, T., Hanson, E.M., Boomer, I., Kirby, N., 2022. Data report: Cenozoic and Upper Cretaceous bulk carbonate stable carbon and oxygen isotopes from IODP Expedition 369 Sites U1513, U1514, and U1516 in the southeast Indian Ocean, in: Hobbs, R.W., Huber, B.T., Bogus, K.A., the Expedition 369 Scientists (Eds.), Australia Cretaceous Climate and Tectonics: Proceedings of the International Ocean Discovery Program. International Ocean Discovery Program, College Station, TX, https://doi.org/10.14379/iodp.proc.369.206.2022.

Evans, D., Sagoo, N., Renema, W., Cotton, L.J., Müller, W., Todd, J.A., Saraswati, P.K, Stassen, P., Ziegler, M., Pearson, P.N., Valdes, P.J, Affek H.P., 2018. Eocene greenhouse climate revealed by coupled clumped isotope Mg/Ca thermometry. Proc. Natl. Acad. Sci. U S A. 115, 1174–1179. https://doi.org/10.1073/pnas.1714744115.

Fleet, A.J., McKelvey, B.C., 1978. Eocene explosive submarine volcanism, Ninetyeast Ridge, Indian Ocean. Mar. Geol. 26, 73–97.

Gong, Q., Wang, X., Zhao, L., Grasby, S.E., Chen, Z.-Q., Zhang, L., Li, Y., Cao, L., Li, Z., 2017. Mercury spikes suggest volcanic driver of the Ordovician-Silurian mass extinction. Sci. Rep. 7, 5304

Grasby, S.E., Beauchamp, B., Bond, D.P.G., Wignall, P.B., Sanei, H., 2016. Mercury anomalies associated with three extinction events (Capitanian Crisis, latest Permian Extinction and the Smithian/Spathian Extinction) in NW Pangea. Geol. Mag. 153, 285–297.

Grasby, S.E., Shen, W., Yin, R., Gleason, J.D., Blum, J.D., Lepak, R.F., Hurley, J.P., Beauchamp, B., 2017. Isotopic signatures of mercury contamination in latest Permian oceans. Geology 45, 55–58.

Grasby, S.E., Them II, T.R., Chen, Z., Yin, R., Ardakani, O.H., 2019. Mercury as a proxy for volcanic emissions in the geologic record. Ear. Sci. Rev. 196, 102880. https://doi.org/10.1016/j.earscirev.2019.102880.

Henehan, M.J., Edgar, K.M., Foster, G.L., Penman, D.E., Hull, P.M., Greenop, R., Anagnostou, E., Pearson, P., 2020. Revisiting the Middle Eocene Climatic Optimum "Carbon Cycle Conundrum" with new estimates of atmospheric pCO_2 from boron isotopes. Paleoceanogr. Paleoclimatol. 35, e2019PA003713. https://doi.org/10.1029/2019PA003713.

Inglis, G. N., Farnsworth, A., Lunt, D., Foster, G. L., Hollis, C. J., Pagani, M., Jardine, P. E., Pearson, P. N., Markwick, P., Galsworthy, A. M. J., et al., 2015. Descent toward the Icehouse: Eocene sea surface cooling inferred from GDGT distributions, Paleoceanography, 30, 1000–1020, doi:10.1002/2014PA002723.

Jones, J.B., and Fitzgerald, M.J., 1984. Extensive volcanism associated with the separation of Australia and Antarctica. Science 226, 346–348. https://doi.org/10.1126/science.226.4672.346.

Kim, J., Lim, D., Jeong, D., Xu, Z., Kim, H., Kim, J., 2022. Mercury (Hg) geochemistry of mid-ocean ridge sediments on the Central Indian Ridge: Chemical forms and isotopic composition. Chem. Geol. 604, 120942. https://doi.org/10.1016/j.chemgeo.2022.120942.

Klemm, V., Levasseur, S., Frank, M., Hein, J.R., Halliday, A.N., 2005. Osmium isotope stratigraphy of a marine ferromanganese crust. Earth Planet. Sci. Lett. 238, 42–48.

Li. Q., James, N.P., McGowran, B., 2003. Middle and Late Eocene Great Australian Bight lithobiostratigraphy and stepwise evolution of the southern Australian continental margin. Aust.

J. Earth Sci. 50, 113–128.

Lu, X., Kendall, B., Stein, H.J., Hannah, J.L., 2017. Temporal record of osmium concentrations and $^{187}Os/^{188}Os$ in organic-rich mudrocks: implications for the osmium geochemical cycle and the use of osmium as a paleoceanographic tracer. Geochim. Cosmochim. Acta 216, 221–241.

Martin, H.A., 2006. Cenozoic climatic change and the development of the arid vegetation in Australia. J. Arid Environ. 66, 533–563. https://doi.org/10.1016/j.jaridenv.2006.01.009.

Matsumoto, H., Coccioni, R., Frontalini, F., Shirai, K., Jovane, L., Trindade, R., Safian, J.F., Kuroda, J., 2022. Mid-Cretaceous marine Os isotope evidence for heterogeneous cause of oceanic anoxic events. Nat. Comm. 13, 239.

Moynier, F., Jackson, M.G., Zhang, K., Cai, H., Halldórsson, S.A., Pik, R., Day, J.M.D., Chen, J., 2021. The mercury isotopic composition of earth's mantle and the use of mass independently fractionated Hg to test for recycled crust. Geophys. Res. Lett. 48, e2021GL094301. https://doi.org/10.1029/2021GL094301.

Müller, R.D., Seton, M., Zahirovic, S., Williams, S.E., Matthews, K.J., Wright, N.M., Shephard, G.E., Maloney, K.T., Barnett-Moore, N., Hosseinpour, M., Bower, D.J., Cannon, J., 2016. Ocean basin evolution and global-scale plate reorganization events since Pangea Breakup. Annu. Rev. Earth Planet. Sci. 44, 107–138. https://doi.org/10.1146/annurev-earth-060115-012211.

Niyazi, Y., Eruteya, O.E., Warne, M., Ierodiaconou, D., 2021. Discovery of large-scale buried volcanoes within the Cenozoic succession of the Prawn Platform, offshore Otway Basin, southeastern Australia. Mar. Petrol. Geol. 123. 104747.

Paquay, F.S., Ravizza, G.E., 2012. Heterogeneous seawater $^{187}Os/^{188}Os$ during the late Pleistocene glaciations. Earth. Planet. Sci. Lett. 349–350, 126–138.

Penman, D.E., Rugenstein, J.K.C., Ibarra, D.E., Winnick, M.J., 2020. Silicate weathering as a feedback and forcing in Earth's climate and carbon cycle. Ear. Sci. Rev. 209, 103298. https://doi.org/10.1016/j.earscirev.2020.103298.

Percival, L.M.E., Cohen, A.S., Davies, M.K, Dickson, A.J., Hesselbo, S.P., Jenkyns, H.C., Leng, M.J., Mather, T.A., Storm, M.S., Xu, W., 2016. Osmium isotope evidence for two pulses of increased continental weathering linked to Early Jurassic volcanism and climate change. Geology 44, 759–762. https://doi.org/10.1130/G37997.1.

Percival, L.M.E., Jenkyns, H.C., Mather, T.A., Dickson, A.J., Batenburg, S.J., Ruhl, M., Hesselbo,

S.P., Barclay, R., Jarvis, I., Robinson, S.A., Woelders L., 2018. Does large igneous province volcanism always perturb the mercury cycle? Comparing the records of Oceanic Anoxic Event 2 and the End-Cretaceous to other Mesozoic events. Am. J. Sci. 318, 799–860. https://doi.org/10.2475/08.2018.01.

Peucker-Ehrenbrink, B., Ravizza, G., 2000. The marine osmium isotope record. Terra Nova 12, 205–219. https://doi.org/10.1046/j.1365-3121.2000.00295.x.

Ravizza, G., Norris, R.N., Blusztajn, J., 2001. An osmium isotope excursion associated with the late Paleocene thermal maximum: Evidence of intensified chemical weathering. Paleoceanography 16, 155-163.

Rea D.K., Zachos, J.C., Owen, R.M., Gingerich, P.D., 1990. Global change at the Paleocene-Eocene boundary: climatic and evolutionary consequences of tectonic events. Paleogeogr. Paleoclimatol. Paleoecol. 79, 117–128.

Rivero-Cuesta, L., Westerhold, T., Alegret, L., 2020. The Late Lutetian Thermal Maximum (middle Eocene): first record of deep-sea benthic foraminiferal response. Palaeogeogr. Palaeoclimatol. Palaeoecol. 545, 109637. https://doi.org/10.1016/j. palaeo.2020.109637.

Rolewicz, Z.L., 2013. Seawater Osmium Isotope Records From Pacific ODP and IODP Sites - Refining the Paleogene Curve and Dating Red Clay Sequences. Undergraduate research scholars Thesis. Texas A&M University.

Royer, J-Y., Sandwell, D.T., 1989. Evolution of the eastern Indian Ocean since the Late Cretaceous: Constraints from Geosat altimetry. J. Geophys. Res. Solid Earth 94, 13755–13782. https://doi.org/10.1029/JB094iB10p13755.

Rudnick, R.L., Gao, S., 2014. Composition of the continental crust, in: Holland, H.D., Turekian, K.K. (Eds.), Treatise on Geochemistry, 2nd ed. Elsevier, Oxford, pp. 1–51.

Shen, J. Algeo, T.J., Feng, Q., 2022. Mercury isotope evidence for a non-volcanic origin of Hg spikes at the Ordovician-Silurian boundary, South China. Earth Planet. Sci. Lett. 594, 117705. https://doi.org/10.1016/j.epsl.2022.117705.

Shen, J., Algeo, T.J., Planavsky, N.J., Yu, J., Feng, Q., Song, H.J., Song, H., Rowe, H., Zhou, L., Chen, J., 2019. Mercury enrichments provide evidence of Early Triassic volcanism following the End-Permian mass extinction. Ear. Sci. Rev. 195, 191–212.

Shen, J., Chen J., Yu, J., Algeo, T.J., Smith, R.M.H., Botha, J., Frank, T.D., Fielding, C.R., Ward, P.D., Mather, T.A., 2023. Mercury evidence from southern Pangea terrestrial sections for end-

Permian global volcanic effects. Nat. Commun. 16, 6. https://doi.org/10.1038/s41467-022-35272-8.

Shen, J., Feng, Q., Algeo, T.J., Liu, J., Zhou, C., Wei, W., Liu, J., Them, T.R., Gill, B.C., Chen, J., 2020. Sedimentary host phases of mercury (Hg) and implications for use of Hg as a volcanic proxy. Earth Planet. Sci. Lett. 543, 116333.

Sherman, L.S., Blum, J.D., Nordstrom, D.K., McCleskey, R.B., Barkay, T., Vetriani, C., 2009. Mercury isotopic composition of hydrothermal systems in the Yellowstone Plateau volcanic field and Guaymas Basin sea-floor rift. Earth Planet. Sci. Lett. 279, 86–96.

Sial, A.N., Chen, J., Lacerda, L.D., Frei, R., Tewari, V.C., Pandit, M.K., Gaucher, C., Ferreira, V.P., Cirilli, S., Peralta, S., Korte, C., Barbosa, J.A., Pereira, N.S., 2016. Mercury enrichment and Hg isotopes in Cretaceous–Paleogene boundary successions: Links to volcanism and palaeoenvironmental impacts. Cretac. Res. 66, 60–81,

Sial, A.N., Chen, J., Lacerda, L.D., Korte, C., Spangenberg, J.E., Silva-Tamayo, J.C., Gaucher, C., Ferreira, V.P., Barbosa, J.A., Pereira, N.S., Benigno, A.P., 2020. Globally enhanced Hg deposition and Hg isotopes in sections straddling the Permian-Triassic boundary: link to volcanism. Paleogeogr. Paleoclimatol. Paleoecol. 540, 109537. https://doi.org/10.1016/j.palaeo.2019.109537.

Sluijs, A., Zeebe, R.E., Bijl, P.K., Bohaty, S.M., 2013. A middle Eocene carbon cycle conundrum. Nat. Geosci. 6, 429–434. https://doi.org/10.1038/ngeo1807

Štrok, M., Baya, P.A., Hintelmann, H., 2015. The mercury isotope composition of Arctic coastal seawater. C. R. Geosci. 347, 368–376. https://doi.org/10.1016/j.crte.2015.04.001.

Tremblin, M., Hermoso, M., Minoletti, F., 2016. Equatorial heat accumulation as a long-term trigger of permanent Antarctic ice sheets during the Cenozoic. Proc. Natl Acad. Sci. U S A. 113, 11782–11787. www.pnas.org/cgi/doi/10.1073/pnas.1608100113.

van der Boon, A., Kuiper, K.F., van der Ploeg, R., Cramwinckel, M.J., Honarmand, M, Sluijs, A., Krijgsman, W., 2021. Exploring a link between the Middle Eocene Climatic Optimum and Neotethys continental arc flare-up. Clim. Past 17, 229–239. https://doi.org/10.5194/cp-17-229-2021.

van der Ploeg, R., Selby, D., Cramwinckel, M.J., Li, Y., Bohaty, S.M. Middelburg, J.J., Sluijs, A., 2018. Middle Eocene greenhouse warming facilitated by diminished weathering feedback. Nat. Commun. 9, 2877. https://doi.org/10.1038/s41467-018-05104-9.

Veevers, J.J., 2000. Change of tectono-stratigraphic regime in the Australian plate during the 99 Ma (mid-Cretaceous) and 43 Ma (mid-Eocene) swerves of the Pacific. Geology 28, 47–50. https://doi.org/10.1130/0091-7613(2000)28<47:COTRIT>2.0.CO;2.

Vilacis, B., Hayek, J.N., Stotz, I.L., Bunge, H.P., Friedrich, A.M., Carena, S., Clark, S., 2022. Evidence for active upper mantle flow in the Atlantic and Indo-Australian realms since the Upper Jurassic from hiatus maps and spreading rate changes. Proc. Math. Phys. Eng. Sci. 478, 20210764.

Wang, W., Colin, C., Xu, Z., Lim, D., Wan, S., Li, T., 2022. Tectonic and climatic controls on sediment transport to the Southeast Indian Ocean during the Eocene: New insights from IODP Site U1514. Glob. Planet. Change 217, 103956. https://doi.org/10.1016/j.gloplacha.2022.103956.

Wang, F., Zheng, X-S., Lee, J.I.K., Choe, W., Evans, N., Zhu, R-X., 2009. An $^{40}Ar/^{39}Ar$ geochronology on a mid-Eocene igneous event on the Barton and Weaver peninsulas: Implications for the dynamic setting of the Antarctic Peninsula. Geochem. Geophys. Geosyst. 10. Q12006. https://doi.org/10.1029/2009GC002874.

Westerhold, T., Röhl, U., Donner, B., Frederichs, T., Kordesch, W.E.C., Bohaty, S.M., Hodell, D.A., Laskar, J., Zeebe, R.E., 2018. Late Lutetian Thermal Maximum—Crossing a thermal threshold in Earth's climate system? Geochem. Geophys. Geosyst. 19, 73–82. https://doi.org/10.1002/2017GC007240.

Westerhold, T., Marwan, N., Drury, A.J., Liebrand, D., Agnini C., et al., 2020. An astronomically dated record of Earth's climate and its predictability over the last 66 million years. Science 369, 1381–1387. https://doi.org/10.1126/science.aba6853.

Yin, R., Chen, D., Pan, X., Deng, C., Chen, L., Song, X., Yu, S., Zhu, C., Wei, X., Xu, Y., Feng, X., Blum. J., Lehmann, B., 2022. Mantle Hg isotopic heterogeneity and evidence of oceanic Hg recycling into the mantle. Nat. Commun. 13, 948. https://doi.org/10.1038/s41467-022-28577-1

Yin, R., Krabbenhoft, D.P., Bergquist, B., Zheng, W., Lepak, R., Hurley, J., 2016. Effects of mercury and thallium concentrations on high precision determination of mercury isotopic composition by Neptune Plus multiple collector inductively coupled plasma mass spectrometry. J. Anal. At. Spectrom. 31, 2060–2068. https://doi.org/10.1039/C6JA00107F.

Zambardi, T., Sonke, J.E., Toutain, J.P., Sortino, F., Shinohara, H., 2009. Mercury emissions and stable isotopic compositions at Vulcano Island (Italy). Earth Planet. Sci. Lett. 277, 236–243.

https://doi.org/10.1016/j.epsl.2008.10.023.

Zachos, J.C., Pagani, M., Sloan, L.C., Thomas, E., Billups, K., 2001. Trends, rhythms, and aberrations in global climate 65 Ma to present. Science 292, 689–693. http://dx.doi.org/10.1126/science.1059412.

Figure captions

Figure 1. (A) Paleo- (~40 Ma) and (B) present-location of IODP 369 Site U1514. Shown in a paleogeographic reconstruction are other drilled core sites (ODP Site 865, Rolewicz, 2013; ODP Site 959 and 1263, and IODP Site U1333, van der Ploeg et al., 2018) and manganese crust section (CD29-2, Klemm et al., 2005) cited for comparison of osmium isotope data. The basic map of paleogeographic reconstruction is from van der Ploeg et al. (2018).

Figure 2. The lithology, linear sedimentation rate, and age-depth plot of sediments between 56 and 260 m CCSF at Site U1514 (after Wang et al., 2022). Age determinations are based the geological time scale 2012 (GTS2012). E. Eoc.: early Eocene, L. Eoc.: late Eocene, Olig.: Oligocene.

Figure 3. Vertical profiles of (A) Hg concentrations and their ratios normalized by (B) TOC and TIC, (C) Al and TS contents, (D) Hg isotope (Δ^{199}Hg), (E) ^{192}Os concentrations, and (F) initial ^{187}Os/^{188}Os (Os$_i$) for bulk sediments of Site U1514. Vertical dashed lines indicate the baseline values (average values of early and late Eocene intervals). Four climax episodes of volcanic eruptions are shown as gray shaded vertical bars near y-axis. Os*i* data of CD29-2 (Klemm et al., 2005) is incorporated into Figure (F) for comparison.

Figure 4. Vertical profiles of (A) Hg/TOC ratio, (B) EF_{Hg}, (C) Hg flux, (D) Hg isotope (Δ^{199}Hg), (E) bulk carbon isotope (δ^{13}C) for Site U1514, and (F) major tectonic and volcanic events. Bulk carbon isotope data for Site U1514 are from Edgar et al. (2022). Note the volcanic climax episode that lasted ~1.5 Myr, just before the MECO. Horizontal dashed lines indicate submarine volcanic climax episodes coupled with low Δ^{199}Hg values. 1) Cottin et al. (2011), 2) Borrissova et al. (2010), 3) Veevers (2000), 4) Vilacis et al. (2022), 5) Niyazi et al. (2021), 6) van der Boon et al., (2021). LLTM: Late Lutetian Thermal Maximum, MECO: Middle Eocene Climate Optimum, KP: Kerguelen Plateau, BR: Broken Ridge, SE AUS: Southeastern Australian Continent, ANT: Antarctica

Figure 5. Cross-plot of Δ^{199}Hg versus Hg concentration and enrichment (Hg/TOC) for Site U1514. The values of Δ^{199}Hg for mantle-derived volcanic emissions (0.00 ± 0.05‰, 2σ) and seawater (+0.21 ± 0.07‰, 2σ) are from Moynier et al. (2021) and Štrok et al. (2015), respectively.

Figure 6. Temporal variations of (A) Os isotopic ratio (Os_i), (B) mass accumulation rate ($MAR_{siliciclastic}$) of detrital materials, (C) chemical weathering indices (kaolinite/smectite ratio and Mg/Al ratio) for Site U1514, and (D) the global deep-sea (Westerhold et al., 2020) and Austral high latitude surface temperatures (Tremblin et al., 2016). Note synchronous increase in Os_i and chemical weathering indices during the middle Eocene (especially the MECO). The data of chemical weathering indices for U1514 and Os_i values for Site 1264 (see Fig. 1a for core site) are from Wang et al. (2022) and van der Ploeg et al. (2018), respectively. The middle Eocene warming reversal is shown as the shaded area.

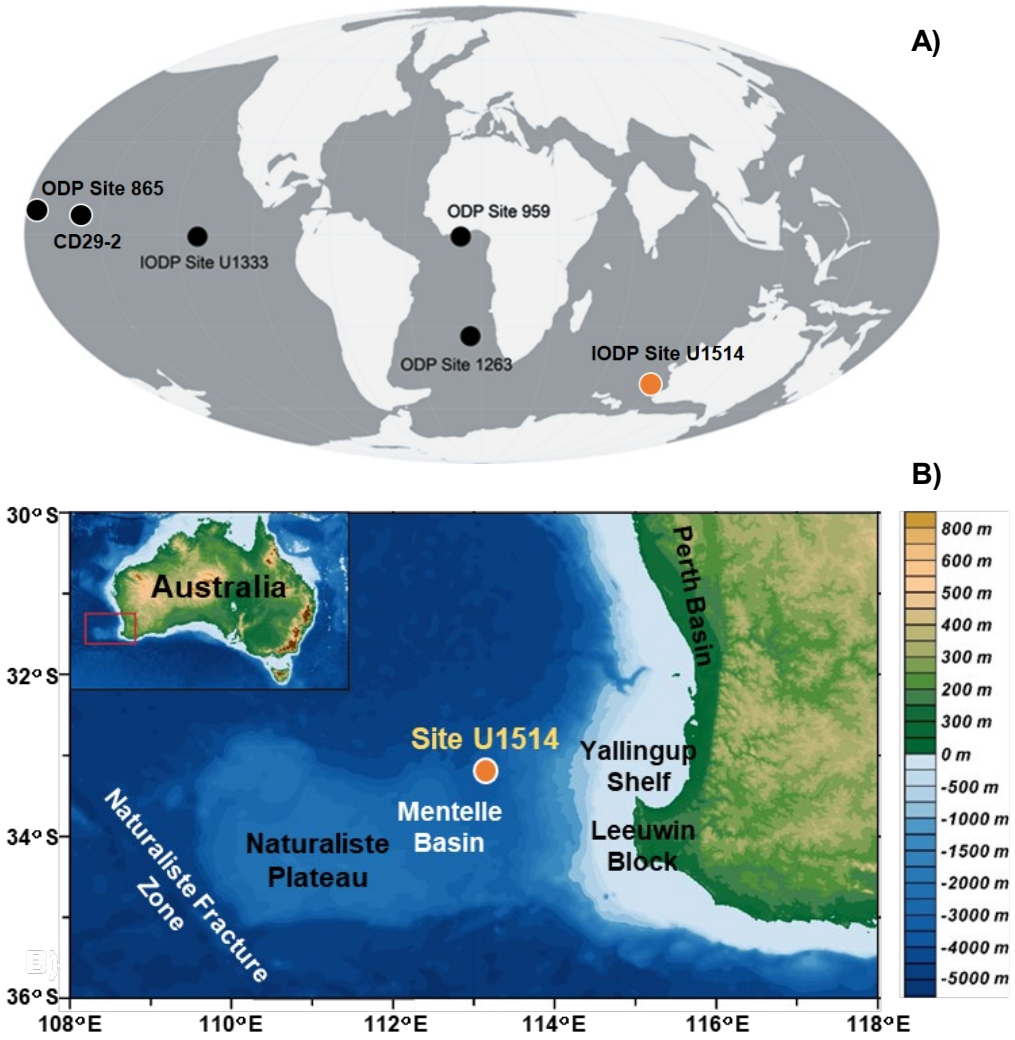
A)
ODP Site 865
CD29-2
IODP Site U1333
ODP Site 959
ODP Site 1263
IODP Site U1514
B)
Australia
Perth Basin
Site U1514
Yallingup Shelf
Mentelle Basin
Leeuwin Block
Naturaliste Plateau
Naturaliste Fracture Zone
30° S
32° S
34° S
36° S
108°E
110°E
112°E
114°E
116°E
118°E
800 m
600 m
500 m
400 m
300 m
200 m
300 m
0 m
-500 m
-1000 m
-1500 m
-2000 m
-3000 m
-4000 m
-5000 m

Figure 1.

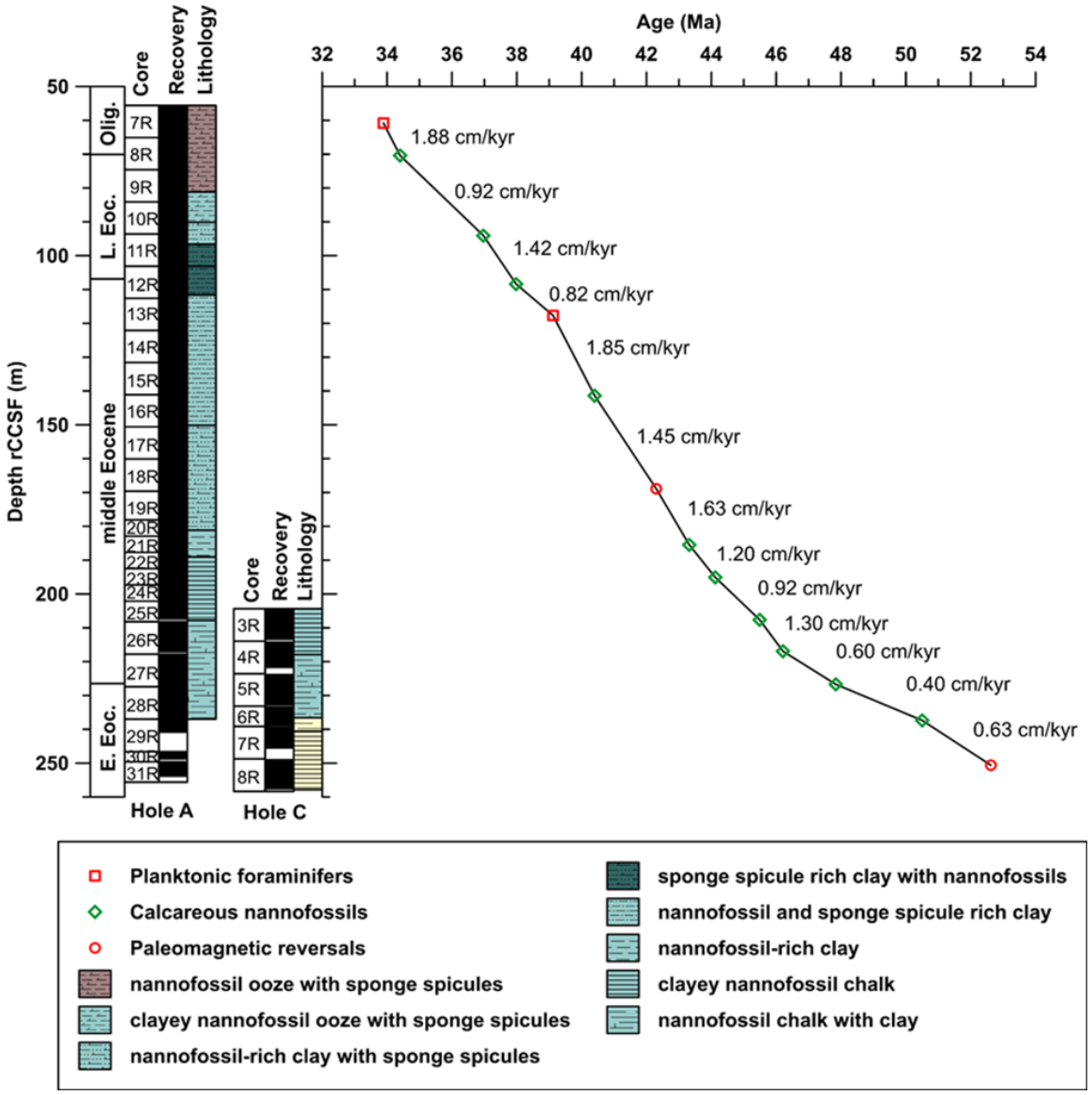
Age (Ma)
32
34
36
38
40
42
44
46
48
50
52
54
Depth rCCSF (m)
50
100
150
200
250
Olig.
L. Eoc.
middle Eocene
E. Eoc.
Core
Recovery
Lithology
7R
8R
9R
10R
11R
12R
13R
14R
15R
16R
17R
18R
19R
20R
21R
22R
23R
24R
25R
26R
27R
28R
29R
30R
31R
Hole A
3R
4R
5R
6R
7R
8R
Hole C
1.88 cm/kyr
0.92 cm/kyr
1.42 cm/kyr
0.82 cm/kyr
1.85 cm/kyr
1.45 cm/kyr
1.63 cm/kyr
1.20 cm/kyr
0.92 cm/kyr
1.30 cm/kyr
0.60 cm/kyr
0.40 cm/kyr
0.63 cm/kyr
Planktonic foraminifers
Calcareous nannofossils
Paleomagnetic reversals
nannofossil ooze with sponge spicules
clayey nannofossil ooze with sponge spicules
nannofossil-rich clay with sponge spicules
sponge spicule rich clay with nannofossils
nannofossil and sponge spicule rich clay
nannofossil-rich clay
clayey nannofossil chalk
nannofossil chalk with clay

Figure 2.

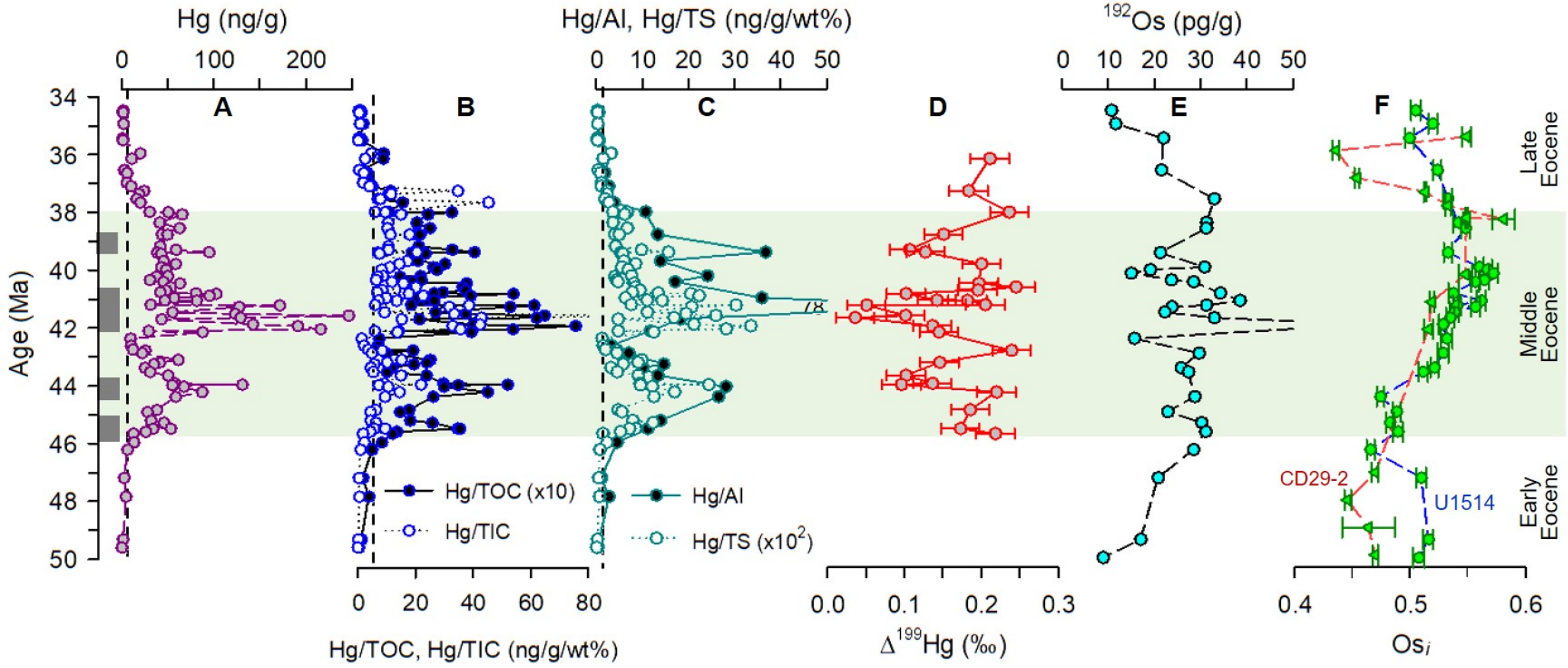
Hg (ng/g)
0
100
200
A
Age (Ma)
34
36
38
40
42
44
46
48
50
B
Hg/TOC (x10)
Hg/TIC
0
20
40
60
80
Hg/TOC, Hg/TIC (ng/g/wt%)
Hg/Al, Hg/TS (ng/g/wt%)
0
10
20
30
40
50
C
Hg/Al
Hg/TS (x10^2)
D
0.0
0.1
0.2
0.3
Δ^{199}Hg (‰)
^{192}Os (pg/g)
0
10
20
30
40
50
E
F
CD29-2
U1514
0.4
0.5
0.6
Os$_i$
Late Eocene
Middle Eocene
Early Eocene

Figure 3.

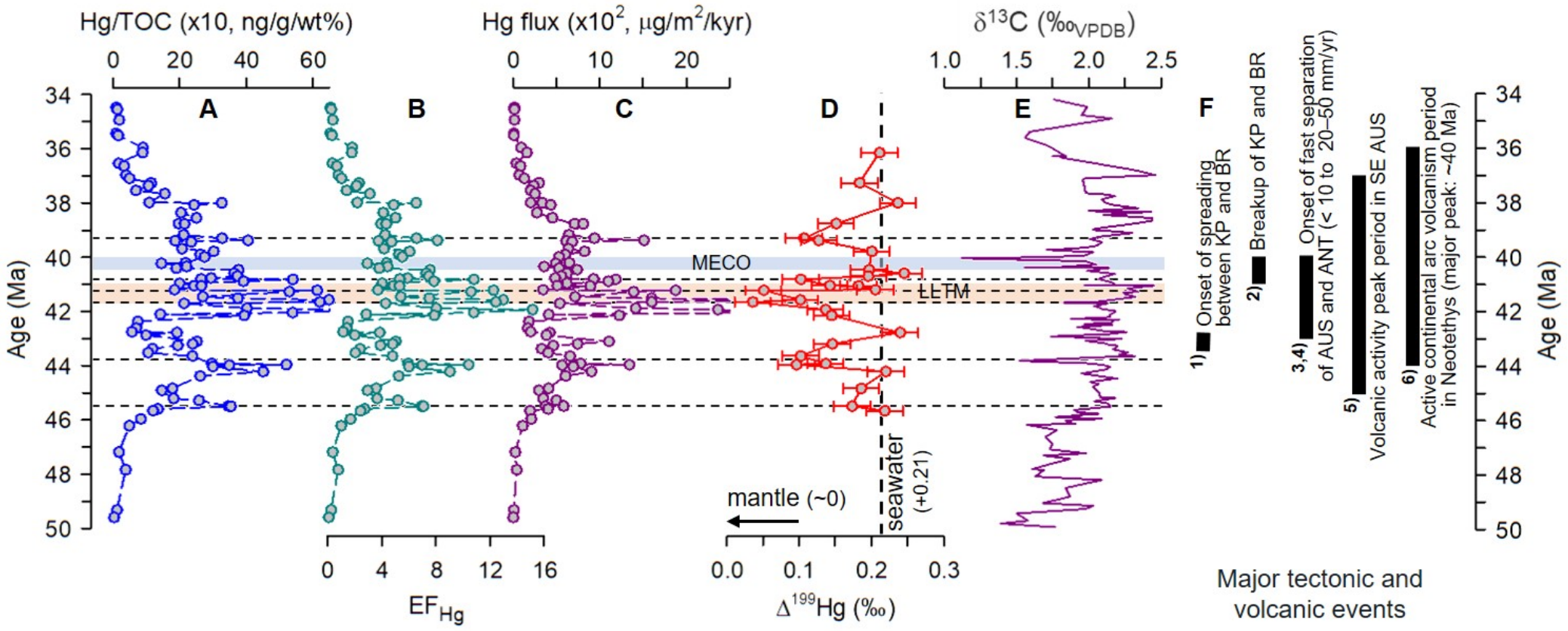
Hg/TOC (x10, ng/g/wt%)
Hg flux (x10², µg/m²/kyr)
δ13C (‰VPDB)
A
B
C
D
E
F
Age (Ma)
MECO
LLTM
mantle (~0)
seawater (+0.21)
EFHg
Δ199Hg (‰)
1) Onset of spreading between KP and BR
2) Breakup of KP and BR
3,4) Onset of fast separation of AUS and ANT (< 10 to 20–50 mm/yr)
5) Volcanic activity peak period in SE AUS
6) Active continental arc volcanism period in Neotethys (major peak: ~40 Ma)
Major tectonic and volcanic events

Figure 4.

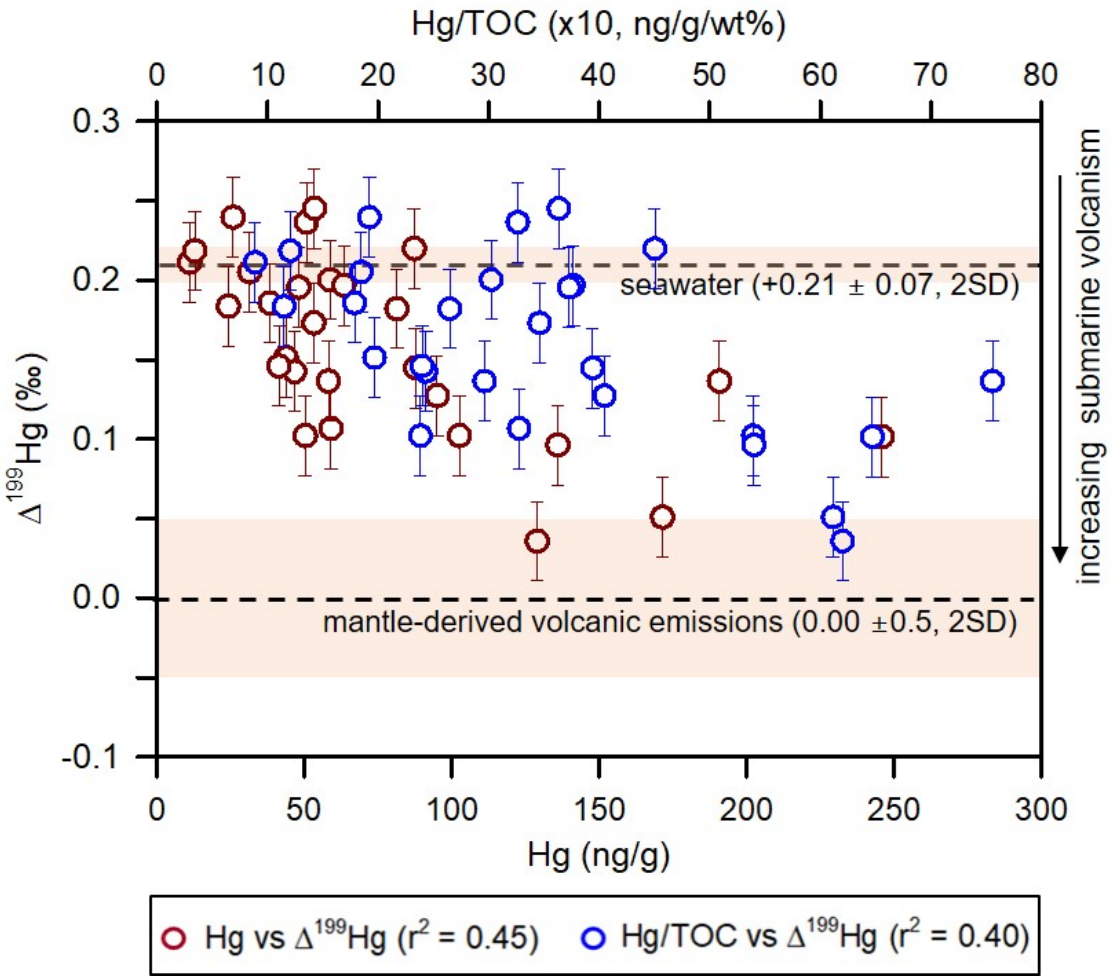
Hg/TOC (x10, ng/g/wt%)
0
10
20
30
40
50
60
70
80
0.3
0.2
0.1
0.0
-0.1
Δ199Hg (‰)
seawater (+0.21 ± 0.07, 2SD)
mantle-derived volcanic emissions (0.00 ±0.5, 2SD)
increasing submarine volcanism
0
50
100
150
200
250
300
Hg (ng/g)
Hg vs Δ199Hg (r2 = 0.45)
Hg/TOC vs Δ199Hg (r2 = 0.40)

Figure 5.

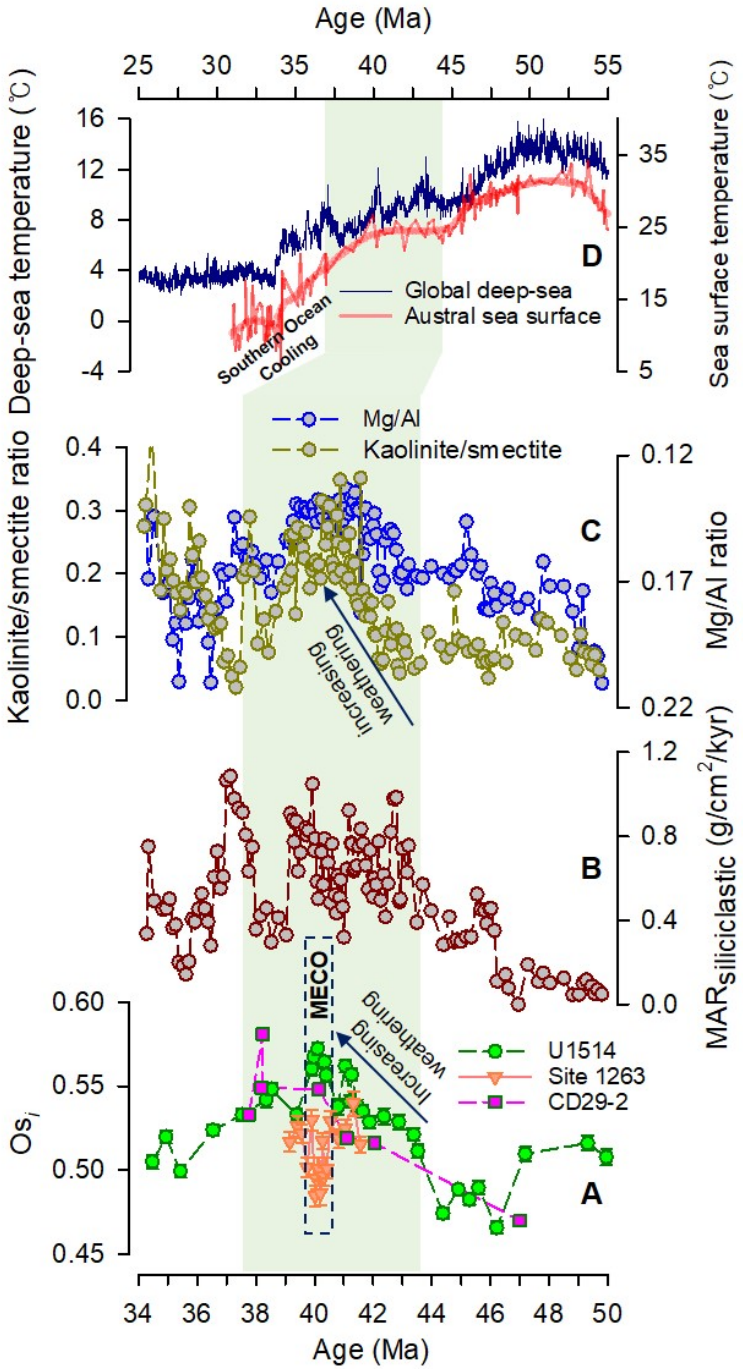
Age (Ma)
25
30
35
40
45
50
55
Deep-sea temperature (℃)
Sea surface temperature (℃)
16
12
8
4
0
-4
35
25
15
5
D
Global deep-sea
Austral sea surface
Southern Ocean Cooling
Mg/Al
Kaolinite/smectite
Kaolinite/smectite ratio
Mg/Al ratio
0.4
0.3
0.2
0.1
0.0
0.12
0.17
0.22
C
Increasing weathering
1.2
0.8
0.4
0.0
B
MECO
Increasing weathering
U1514
Site 1263
CD29-2
Os$_i$
0.60
0.55
0.50
0.45
A
34
36
38
40
42
44
46
48
50
Age (Ma)

Figure 6.